The Astrophysical Journal, 885:111 (15pp), 2019 November 10 https://doi.org/10.3847/1538-4357/ab4808

A BCG with Offset Cooling: Is the AGN Feedback Cycle Broken in A2495?

T. Pasini[1], M. Gitti[1,2], F. Brighenti[1], P. Temi[3], A. Amblard[3,4], S. L. Hamer[5], S. Ettori[6,7], E. O'Sullivan[8], and F. Gastaldello[9]

[1] Dipartimento di Fisica e Astronomia (DIFA), Universita' di Bologna, via Gobetti 93/2, I-40129 Bologna, Italy; myriam.gitti@unibo.it
[2] Istituto Nazionale di Astrofisica (INAF)—Istituto di Radioastronomia (IRA), via Gobetti 101, I-40129 Bologna, Italy
[3] Astrophysics Branch, NASA/Ames Research Center, MS 245-6, Moffett Field, CA 94035, USA
[4] BAER Institute, Sonoma, CA, USA
[5] Department of Physics, University of Bath, Claverton Down, BA2 7AY, UK
[6] Istituto Nazionale di Astrofisica (INAF)—Osservatorio di Astrofisica e Scienza dello Spazio (OAS), via Gobetti 93/3, I-40129 Bologna, Italy
[7] Istituto Nazionale di Fisica Nucleare (INFN)—Sezione di Bologna, viale Berti Pichat 6/2, I-40127 Bologna, Italy
[8] Harvard-Smithsonian Center for Astrophysics, 60 Garden Street, Cambridge, MA 02138, USA
[9] INAF-IASF Milano, via E. Bassini 15, I-20133 Milano, Italy
Received 2019 May 9; revised 2019 September 20; accepted 2019 September 24; published 2019 November 6

Abstract

We present a combined radio/X-ray analysis of the poorly studied galaxy cluster A2495 ($z = 0.07923$) based on new EVLA and *Chandra* data. We also analyze and discuss Hα emission and optical continuum data retrieved from the literature. We find an offset of ∼6 kpc between the cluster brightest cluster galaxy (BCG) (MCG+02-58-021) and the peak of the X-ray emission, suggesting that the cooling process is not taking place on the central galaxy nucleus. We propose that sloshing of the intracluster medium (ICM) could be responsible for this separation. Furthermore, we detect a second, ∼4 kpc offset between the peak of the Hα emission and that of the X-ray emission. Optical images highlight the presence of a dust filament extending up to ∼6 kpc in the cluster BCG and allow us to estimate a dust mass within the central 7 kpc of $1.7 \times 10^5\ M_\odot$. Exploiting the dust-to-gas ratio and the $L_{\rm H\alpha}$–$M_{\rm mol}$ relation, we argue that a significant amount (up to $10^9\ M_\odot$) of molecular gas should be present in the BCG of this cluster. We also investigate the presence of ICM depressions, finding two putative systems of cavities; the inner pair is characterized by $t_{\rm age} \sim 18$ Myr and $P_{\rm cav} \sim 1.2 \times 10^{43}$ erg s^{-1}, the outer one by $t_{\rm age} \sim 53$ Myr and $P_{\rm cav} \sim 5.6 \times 10^{42}$ erg s^{-1}. Their age difference appears to be consistent with the freefall time of the central cooling gas and with the offset timescale estimated with the Hα kinematic data, suggesting that sloshing is likely playing a key role in this environment. Furthermore, the cavities' power analysis shows that the active galactic nucleus energy injection is able to sustain the feedback cycle, despite cooling being offset from the BCG nucleus.

Unified Astronomy Thesaurus concepts: Dust nebulae (413); X-ray sources (1822); Very Large Array (1766); Cooling flows (2028); Intracluster medium (858); Rich galaxy clusters (2005); Abell clusters (9); Hubble Space Telescope (761); X-ray observatories (1819); Extragalactic radio sources (508); Radio continuum emission (1340); Radio galaxies (1343)

1. Introduction

The classical cooling flow model predicted that the intracluster medium (ICM) of cool-core galaxy clusters should cool, condense, and accrete onto the brightest cluster galaxy (BCG), forming stars and producing strong line emission radiation (Fabian et al. 1994). These features are seen in many galaxy clusters, but both at a rate of ∼1%–10% of that expected in the standard model (Peterson & Fabian 2006).

It is now widely recognized that cooling of the central gas is quenched by active galactic nuclei (AGNs) found in the BCGs of clusters (McNamara & Nulsen 2007; Fabian 2012; Gitti et al. 2012). In this "radio-mode" mechanical feedback, radio jets or outflows inflate bubbles (seen as X-ray brightness depressions named *cavities*) and generate shock waves and cold fronts in the hot atmosphere of the cluster (McNamara et al. 2000; Fabian et al. 2006). The AGN is fueled through supermassive black hole (SMBH) accretion of the same gas condensing from the central regions (Soker & Pizzolato 2005; Gaspari et al. 2011, 2013), establishing a feedback loop in which the various components are able to regulate each other. This hypothesis is supported by the correlation between the AGN mechanical power, estimated from the X-ray cavities, and the ICM cooling rate (e.g., Bîrzan et al. 2004; Rafferty et al. 2006).

BCGs at the center of galaxy clusters often host a rich multiphase medium that can extend for tens of kiloparsecs, as revealed by strong line emission from ionized (warm) and molecular (cold) gas (Crawford et al. 1999; McDonald et al. 2010, 2014; Hamer et al. 2016; Russell et al. 2019, and references therein). The warm and cold gas show correlations with each other and with the hot ICM (Crawford et al. 1999; Edge 2001; Hogan et al. 2017; Pulido et al. 2018), which strongly suggest that hot gas cooling (albeit reduced with respect to the classical cooling flow model) is the origin of the observed cold gas. Observations, simulations, and analytic investigations agree that spatially extended cooling is likely to occur in dense cool cores with short cooling times (or cooling time/dynamical time ratio below a certain threshold; e.g., Hogan et al. 2017; Pulido et al. 2018, and references therein). The multiphase medium in cluster cores also reveals a complex dynamics, likely the result of AGN activity and merging events. Chaotic (turbulent) motion and outflows are common (Heckman et al. 1989; Hamer et al. 2016; Russell et al. 2019). It seems reasonable that cold gas inherits the disturbed dynamics from the (low-entropy) hot gas from which it has

Table 1
Radio Observations Properties

Data	P.I.	Project Code	Number of Spw	Channels	Bandwidth	Array	Total Exposure Time
5 GHz (*C* band)	M. Gitti	SC0143	2 (4832–4960 MHz)	64	128 MHz	B	$7^h58^m35^s$
1.4 GHz (*L* band)	M. Gitti	SC0143	2 (1264–1392 MHz)	64	128 MHz	A	$3^h59^m22^s$

cooled (McDonald et al. 2010; McNamara et al. 2016; Gaspari et al. 2018).

In dynamically relaxed systems, we expect the BCG to be at the center of the cluster potential well, as described by the "central galaxy paradigm" (van den Bosch et al. 2005; Cui et al. 2016). In this scenario, the galaxy should be coincident both with the cluster cool-core center (i.e., the X-ray peak) and with the line emission peak. However, in the case of interactions with other clusters or halos, all these components are likely to shift, leading to the production of offsets between them. The connection between offsets and the dynamical state of clusters has been investigated by both observational studies (Katayama et al. 2003; Patel et al. 2006; Rossetti et al. 2016), making use of the current generation of X-ray satellites (e.g., *Chandra* and *XMM-Newton*), and simulations (Skibba et al. 2011). Hudson et al. (2010) studied a sample of 64 cool-core (CC) and non-cool-core (NCC) clusters, finding that objects with a projected distance $>50\ h_{71}^{-1}$ kpc between the BCG and the X-ray peak (12% of the sample) typically show large-scale radio emission, which is believed to be associated with major mergers; these clusters are usually NCC. On the other hand, the vast majority (80%) of CC clusters present an offset $<50\ h_{71}^{-1}$ kpc; among these, only two clusters show large-scale radio emission. A similar study by Sanderson et al. (2009) on a sample of 65 CC clusters found that stronger cool cores are associated with smaller offsets, since more dynamically disturbed objects have likely undergone a stronger merging phase that produced a disruptive impact on the X-ray core. The same trend was confirmed by Mittal et al. (2009). Offsets of the line emission peak are significant for the comprehension of the clusters dynamical evolution, too: detecting 10^4 K gas shifted from the BCG (e.g., Sharma et al. 2004) could suggest that cooling of the ICM is able to reach low temperatures even outside the central galaxy environment (Hamer et al. 2012). In addition, offsets between the Hα and the X-ray peaks were found in A1795 by Crawford et al. (2005) and in several clusters studied in the work by Hamer et al. (2016).

These works have established the correlation between offsets and clusters' dynamical state (e.g., Rossetti et al. 2016), which can therefore be used in order to discriminate between dynamically relaxed and nonrelaxed objects (e.g., Sanderson et al. 2009; Hudson et al. 2010; Mann & Ebeling 2012).

This work is a multifrequency study of A2495. This object was selected from the *ROSAT* Brightest Cluster Sample (BCS; Ebeling et al. 1998) by choosing objects with X-ray fluxes greater than 10^{-11} erg cm^{-2} s^{-1} (1.18×10^{-11} erg cm^{-2} s^{-1} for A2495) and, among these, by selecting those characterized by $L_{\mathrm{H}\alpha} > 10^{40}$ erg s^{-1} from the catalog of Crawford et al. (1999). Following these criteria, we obtained a compilation of 13 objects, including some of the best-studied galaxy clusters (e.g., A1795, A478); among all these objects, A2495 and A1668 were still unobserved by *Chandra*. We thus proposed joint *Chandra*/Very Large Array observations (P.I. Gitti) of these two clusters and were awarded time in *Chandra* cycles 11 and 12. This paper presents our results for A2495, and a forthcoming paper will describe A1668 (T. Pasini et al. 2019, in preparation). A2495 was previously observed by NVSS, which provides an estimate of the 1.4 GHz flux of $F(1.4\ \mathrm{GHz}) = 14.7 \pm 0.6$ mJy, and by TGSS, from which $F(150\ \mathrm{MHz}) \simeq 136$ mJy. We also discuss Hα data from Hamer et al. (2016) and exploit optical images (P.I. Zaritsky) from the *Hubble Space Telescope* (*HST*) archive. With this broad data coverage, we are in the position to perform a multiwavelength investigation of this cluster, which will allow us to better understand the dynamical interactions between the hot ICM, the colder gas, and the radio galaxy hosted in the BCG.

We adopt a ΛCDM cosmology with $H_0 = 73$ km s^{-1} Mpc^{-1} and $\Omega_M = 1 - \Omega_\Lambda = 0.3$ and assume a BCG redshift $z = 0.07923$ (Hamer et al. 2016; Rines et al. 2016) for the cluster as a whole. The luminosity distance is 345 Mpc, leading to a conversion of $1'' = 1.44$ kpc.

2. Radio Analysis

2.1. Observations and Data Reduction

We performed new observations of the radio source associated with A2495 BCG (R.A. $= 22^h50^m19\overset{s}{.}7$, decl. $= +10°54^m12\overset{s}{.}7$, J2000) at 5 and 1.4 GHz with the EVLA in, respectively, B and A configuration (for details, see Table 1).

For both the observations the source 3C 48 (J0137+3309) was used as the primary flux calibrator; for the 5 GHz observation, which was split into two data sets, J2241+0953 was used as the secondary phase calibrator and 3C 48 as the polarization calibrator; for the 1.4 GHz observation, J2330+1100 was used as both the secondary phase and polarization calibrator.

The data reduction was performed with the NRAO Common Astronomy Software Applications package (CASA), version 5.3. We applied the standard calibration procedure on each data set and carried out an accurate editing of the visibilities. We performed both manual and automatic flagging (task `FLAGDATA`, mode = manual and rflag) to exclude radio frequency interferences and corrupted data. As a result, we removed about 10% of the visibilities in the 5 GHz band and about 20% in the 1.4 GHz band. We also attempted the self-calibration on the target, but the operation was not successful, probably due to the source faintness.

We then applied the standard imaging procedure, using the `CLEAN` task, on a $7'' \times 7''$ region centered on the cluster. We made use of the `gridmode=WIDEFIELD` option in order to parameterize the sky curvature; we also set a two-term approximation of the spectral model by using `nterms=2` (MS-MFS algorithm; Rau & Cornwell 2011) and performed a multiscale clean (`multiscale=[0, 5, 24]`), in order to better reconstruct the faint extended emission.

2.2. Results

For each observing band, we produced maps by setting `weighting=BRIGGS` and `ROBUST 0`, in order to obtain the best combination of resolution and sensitivity. The `NATURAL`

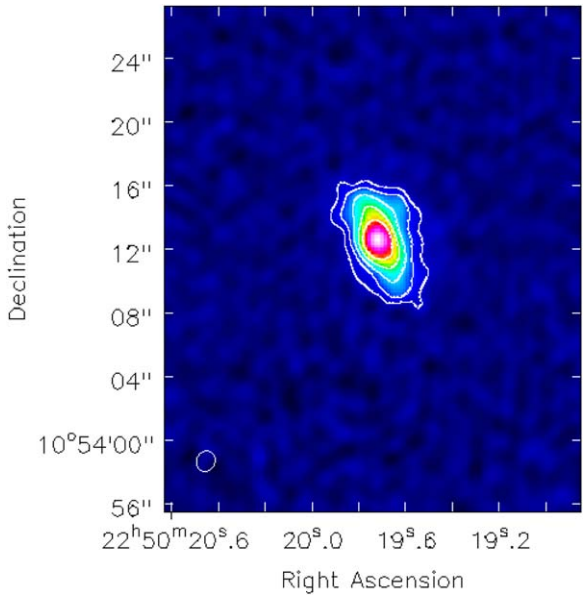

Figure 1. 5 GHz map (ROBUST 0) of A2495. The resolution is $1\farcs30 \times 1\farcs15$, with an rms noise of 4 μJy beam^{-1}. Contours are at -3, 3, 6, 12, 24, 48 $\times$ rms. The source flux is 2.37 $\pm$ 0.19 mJy. The lower left circle represents the beam.

and UNIFORM maps, which respectively enhance the sensitivity and the resolution, did not exhibit any interesting feature compared to the ROBUST 0 image, so they are not shown here. Typical amplitude calibration errors of our data were at 8%: this is the uncertainty we assumed for the flux density measurements.

2.2.1. 5 GHz Map

The 5 GHz map (Figure 1) is characterized by a resolution of $1\farcs30 \times 1\farcs15$ and an rms noise of 4μJy beam^{-1}. The total 5 GHz flux of the radio source in A2495 is 2.37 $\pm$ 0.19 mJy. This result is slightly different from that of Hogan et al. (2015b), who measured a source flux of 2.85 $\pm$ 0.09 mJy in C array. This difference can be produced by either observational or intrinsic effects: the maximum baseline of C configuration, used by Hogan et al. (2015b), is shorter with respect to the B array, and therefore its brightness sensitivity is higher; on the other hand, short-timescale (weeks to months) 10%–30% flux variations in radio galaxies have recently been observed, especially in cool-core cluster's BCGs (e.g., Dutson et al. 2014; Hogan et al. 2015a).

We find that the radio emission is produced by the central radio galaxy on a scale of $\sim$10″; we do not observe any feature of diffuse emission. Following the method described by Feretti & Giovannini (2008), we estimated the equipartition field, finding $B_{\rm eq}(5\ {\rm GHz}) = 3.81 \pm 0.05\ \mu$G, consistent with the typical values characterizing radio galaxies.

We used stokes=Q and stokes=U maps in order to get information about the radio source polarization and found that the polarization percentage at 5 GHz is about 5%. Table 2 summarizes the radio properties of the source on each band.

2.2.2. 1.4 GHz Map

In Figure 2 we overlaid the 1.4 GHz contours on an optical image (F606W filter) retrieved from the *HST* Archive. The total source flux at this frequency is 15.7 $\pm$ 1.3 mJy, in agreement with the estimation made by Owen & Ledlow (1997) of $\sim$14 mJy. The radio source emission entirely lies on the BCG, whose major axis measures $\sim$25 kpc; there are no apparent hints of emission on larger scales. This is confirmed by the lack of additional flux on short baselines and by the flux estimate given by NVSS (see Section 1), consistent with ours. The radio galaxy morphology is very similar to the one at 5 GHz, extending on a scale of about $\sim$10″ ($\sim$14 kpc). Radio properties at 1.4 GHz can be found in Table 2.

The 1.4 GHz luminosity is 2.18×10^{23} W Hz^{-1}: the radio source in A2495 can be classified as an FR I galaxy, characterized by asymmetric lobes and absence of hot spots. Similarly to what was done at 5 GHz, we estimated the equipartition field, finding 5.60 $\pm$ 0.07 μG, and determined an upper limit of $\sim$1% for the polarization. Hogan et al. (2015b) performed a study of the radio properties of a large sample of BCGs, producing the luminosity function at 1.4 GHz of the BCS. Notably, our luminosity estimate places A2495 in the 80th percentile of the function (see Figure 4 of Hogan et al. 2015b); of the 13 clusters that meet our selection criteria, it is the least radio powerful.

2.2.3. Spectral Index Map

We produced the spectral index map, via the CASA task IMMATH, by combining the 1.4 GHz and the 5 GHz ones produced by setting weighting=UNIFORM, uvrange=6-178 (in order to match *uv* ranges between the two bands), with a resolution of $1\farcs1 \times 1\farcs1$. The result is shown in Figure 3.

The synchrotron index α is defined as

$$\alpha = -\frac{\log \frac{S_1}{S_2}}{\log \frac{\nu_1}{\nu_2}}, \quad (1)$$

where, in this work, S_1 and S_2 are, respectively, the 5 GHz flux (hereafter S_C) and the 1.4 GHz flux (hereafter S_L), while ν_1 and ν_2 are the corresponding frequencies. The radio galaxy core, often characterized by $\alpha \sim -0.5$, exhibits $\alpha \simeq -0.9$, while lobes reach $\alpha \simeq -2$. Table 3 summarizes the spectral index properties.

The mean index is -1.39 ± 0.22, in agreement with Hogan et al. (2015b), which determined $\alpha \simeq -1.35$, thus suggesting the presence of an old electronic population.

3. X-Ray Analysis

3.1. Observation and Data Reduction

A2495 has been observed with the *Chandra* Advanced CCD Imaging Spectrometer S (ACIS-S) on 2012 July 17 (ObsID 12876, P.I. Gitti) for a total exposure of $\sim$8 ks. Data were reprocessed with CIAO 4.9 using CALDB 4.2.1. First, the Chandra_repro script performed the bad pixel removal and the instrument error correction; afterward, we removed the background flares and used Blanksky background files, filtered and normalized to the count rate of the source hard X-ray image (9–12 keV), in order to subtract the background. The final exposure time is 7939 s.

We identified and removed point sources using the CIAO tool Wavdetect. Comparing X-ray sources with optical counterparts, we checked the astrometry of the *Chandra* data and found it to be accurate; no registration correction was

Table 2
Radio Properties of A2495

Band	Flux (mJy)	Luminosity[a] (10^{22} W Hz^{-1})	Volume (kpc^3)	Brightness Temperature (K)	Equipartition Field (μG)	Polarization
5 GHz	2.37 ± 0.19	3.3 ± 0.3	616 ± 56	3.7 ± 0.9	3.81 ± 0.05	5%
1.4 GHz	15.70 ± 1.30	21.8 ± 1.8	1112 ± 78	232 ± 49	5.60 ± 0.07	⩽1%

Note. The volume is estimated assuming a prolate ellipsoidal shape, where the axes are $a = 13.6 \pm 1.8$ kpc, $b = 9.3 \pm 1.8$ kpc for the 5 GHz map and $a = 13.6 \pm 1.8$ kpc, $b = 12.5 \pm 1.8$ kpc for the 1.4 GHz map.
[a] Estimated using $L_\nu = 4\pi \cdot (D_L)^2 \cdot F_\nu \cdot (1+z)^{\alpha-1}$, where D_L is the luminosity distance, F_ν is the flux at the frequency ν, and α is the mean spectral index (see Section 2.2.3).

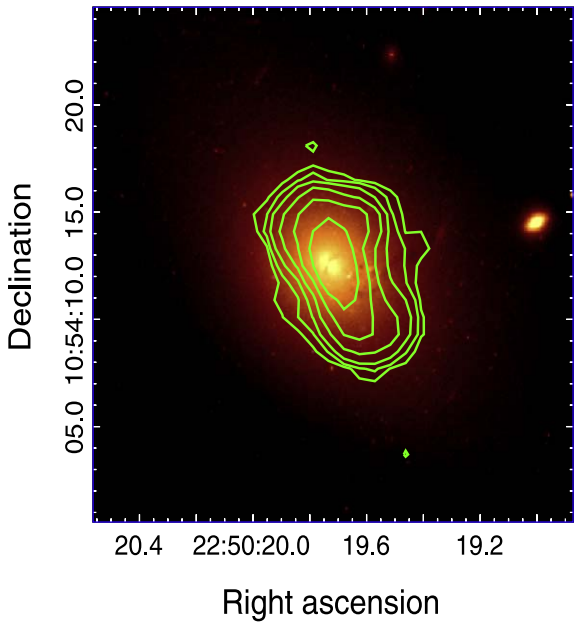

Figure 2. 1.4 GHz contours (ROBUST 0) of the radio source overlaid on an *HST* image (F606W filter) of A2495. The resolution of the radio map is $1\farcs29 \times 1\farcs12$, with an rms noise of 10 μJy beam^{-1}. Contours are at −3, 3, 6, 12, 24, 48 × rms. The source flux is 15.7 ± 1.3 mJy.

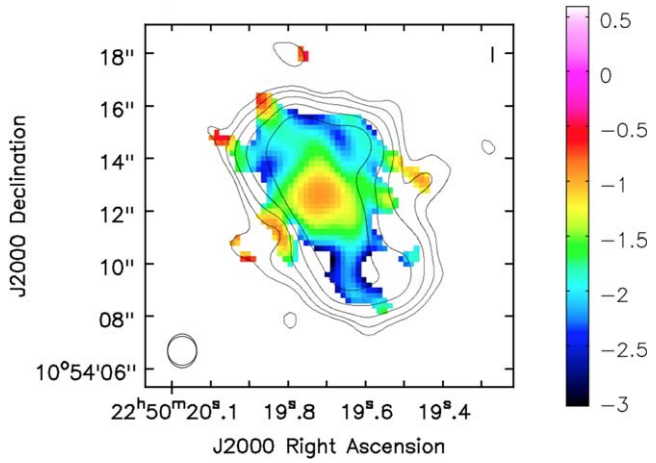

Figure 3. Spectral index map of A2495 between 5 and 1.4 GHz. Contours are the same as in the 1.4 GHz map, and typical errors range from $\Delta\alpha \simeq 0.2$ to $\Delta\alpha \simeq 0.6$ for the inner and outer regions, respectively.

necessary. Unless otherwise stated, the reported errors are at 68% (1σ) confidence level.

3.2. Results

3.2.1. Surface Brightness Profile

Figure 4 shows the smoothed 0.5–2 keV image of A2495. We produced a background-subtracted, exposure-corrected image and then extracted the surface brightness profile from a series of 2″-width concentric annuli centered on the X-ray peak.

We used Sherpa in order to fit this profile in the outer radii (⩾30″) with a single β-model (Cavaliere & Fusco-Femiano 1976) and then extrapolated it to the inner regions. The best-fit values are $\mathtt{r0} = 15\farcs9 \pm 0\farcs9$, $\mathtt{beta} = 0.46 \pm 0.01$, and $\mathtt{ampl} = 0.41 \pm 0.02$ counts s^{-1} cm^{-2} sr^{-1}; the ratio between the χ^2 and the degrees of freedom (dof) is $\chi^2/\mathrm{dof} \simeq 1.59$. The result is represented with the blue line in Figure 5.

We can clearly note the brightness excess characterizing the central regions of cool-core clusters. We therefore fitted a double β-model (Mohr et al. 1999; LaRoque et al. 2006) on the entire radial range. In this case, the best-fit parameters are $\mathtt{r0}_1 = 2.74^{+4.55}_{-1.63}$ arcsec, $\mathtt{beta}_1 = 0.64^{+1.61}_{-0.25}$, and $\mathtt{ampl}_1 = 1.09^{+0.55}_{-0.24}$ counts s^{-1} cm^{-2} sr^{-1} for the first β-model and $\mathtt{r0}_2 = 20.3^{+6.1}_{-2.1}$ arcsec, $\mathtt{beta}_2 = 0.48^{+0.06}_{-0.01}$, and $\mathtt{ampl}_2 = 0.31^{+0.04}_{-0.11}$ counts s^{-1} cm^{-2} sr^{-1} for the second β-model. χ^2/DoF is 1.05. The corresponding model line is shown in red in Figure 5. This suggests that A2495 is, indeed, a cool-core cluster, as expected from the selection criteria exploited for the cluster choice.

3.2.2. Spectral Analysis

We extracted and fitted spectra of A2495 in the 0.5–7 keV band via Xspec (vv.12.9.1), excluding data above 7.0 keV and below 0.5 keV in order to prevent, respectively, contamination from the background and calibration uncertainties. We derived the global cluster properties extracting a spectrum from a ∼200″ circular region centered on the X-ray peak (located at R.A. = $22^{\mathrm{h}}50^{\mathrm{m}}19\fs4$, decl. = $+10°54^{\mathrm{m}}14\fs2$). The spectrum was then fitted assuming an absorbed emission produced by a collisionally ionized diffuse gas, making use of the wabs*apec model. The hydrogen column density was fixed at $N_{\mathrm{H}} = 4.73 \times 10^{20}$ cm^{-2} (estimated from Kalberla et al. 2005); redshift was fixed at $z = 0.07923$. The only parameters left free to vary were the abundance Z, the temperature kT, and the normalization parameter. We found $kT = 3.90 \pm 0.20$ keV, $Z = 0.54^{+0.11}_{-0.10}\ Z_\odot$, and $F(0.5\text{–}7\ \mathrm{keV}) = 1.07^{+0.01}_{-0.02} \times 10^{-11}$ erg s^{-1} cm^{-2}, leading to a total luminosity in the 0.5–7 keV band of $L(0.5\text{–}7\ \mathrm{keV}) = (1.44 \pm 0.02) \times 10^{44}$ erg s^{-1}.

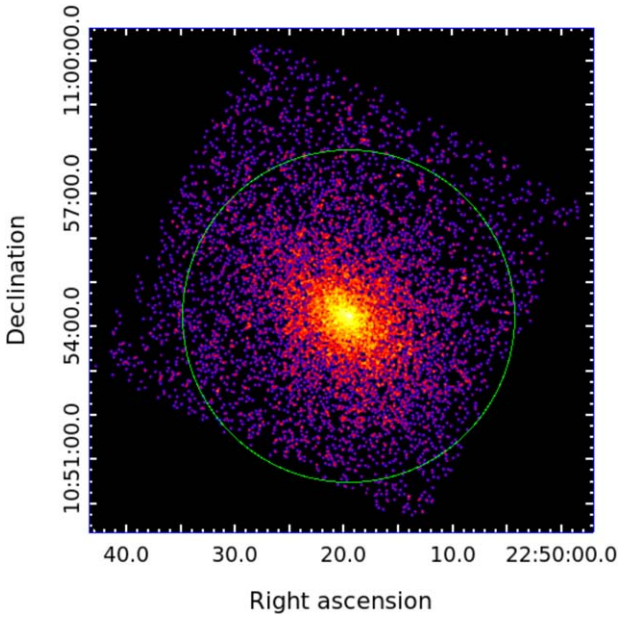

Figure 4. The 0.5–2 keV image of A2495, smoothed with a 5σ Gaussian. The green circle represents the maximum radius considered for the spectral analysis (see Section 3.2.2).

Table 3
Spectral Index Properties

Region	$S_C \pm \Delta S_C$ (mJy)	$S_L \pm \Delta S_L$ (mJy)	$\alpha \pm \Delta\alpha$
Peak	0.77 ± 0.06	2.20 ± 0.18	-0.79 ± 0.08
Extended[a]	1.60 ± 0.16	13.50 ± 1.08	-1.59 ± 0.08
Total	2.37 ± 0.19	15.70 ± 1.26	-1.39 ± 0.22

Note. The second column shows the flux values at 5 GHz, while the third column displays the 1.4 GHz values. The fourth column presents the correspondent spectral index values.
[a] Estimated subtracting the peak contributed from the total flux.

We then performed a projected analysis, using a series of concentric rings covering the entire CCD and centered on the X-ray peak, each of which contains a minimum of 2500 total counts (the maximum radius reached, corresponding to 200″, is visible in Figure 4). Results are listed in Table 4.

The low statistics led to large uncertainties in the measured abundances; therefore, in this work the cluster metallicity will not be discussed.

The projected temperature profile of A2495 is shown in cyan in Figure 6. We carried out the same analysis making use of elliptical rings, but we did not find any significant difference.

In order to account for the projection effects, we performed a deprojection analysis by adopting the `projct` model. For this purpose, we used concentric rings containing at least 3500 total counts. As above, the X-ray peak was excluded. Spectra were fitted using a `projct*wabs*apec` model, in which temperature, abundance, and normalization parameters were left free to vary. Results are listed in Table 5. The deprojected temperature profile of the cluster is shown in black in Figure 6.

In both profiles, the temperature value rises, as expected, moving from the center to the outskirts. The outermost bin of the projected analysis suggests the decline typical of relaxed clusters (Vikhlinin et al. 2005). This is less pronounced in the deprojected profile, where the poor statistics led to larger errors.

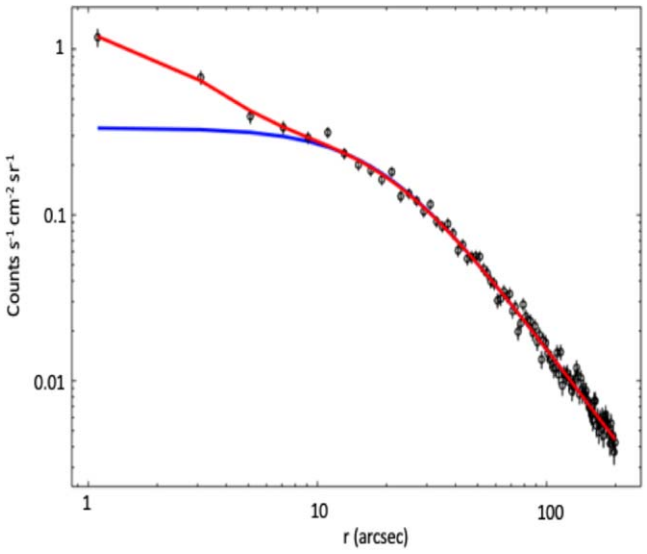

Figure 5. Surface brightness profile of A2495 fitted in the external regions ($\geqslant 30''$) with a single β-model (blue line) and on every radius with a double β-model (red line). The blue line in the inner regions was obtained by extrapolating the model.

The normalization factor $N(r)$ of the `apec` model (see Table 5), if calculated through the deprojection analysis, allows us to obtain an estimate of the electronic density. It is defined as

$$N(r) = \frac{10^{-14}}{4\pi[D_A(1+z)]^2}\int n_e n_p dV, \tag{2}$$

where D_A is the angular distance of the source, calculated as $D_A = D_L/(1+z)^2$, n_e represents the electronic density, n_p represents the proton density, and V is the shell volume. For a collisionally ionized plasma (e.g., Gitti et al. 2012),

$$\int n_e n_p dV \simeq 0.82 n_e^2 V. \tag{3}$$

The electronic density can therefore be estimated as

$$n_e = \sqrt{10^{14}\left(\frac{4\pi \cdot N(r) \cdot [D_A \cdot (1+z)^2]}{0.82 \cdot V}\right)}. \tag{4}$$

Table 5 lists the density values for each shell. The corresponding radial density profile is shown in Figure 7.

From the temperature and density profiles we estimated the cooling time of each region, defined as

$$t_{\rm cool} = \frac{H}{\Lambda(T) n_e n_p} = \frac{\gamma}{\gamma - 1}\frac{kT(r)}{\mu X n_e(r)\Lambda(T)}, \tag{5}$$

where $\gamma = 5/3$ is the adiabatic index, H is the enthalpy, $\mu \simeq 0.61$ is the molecular weight for a fully ionized plasma, $X \simeq 0.71$ is the hydrogen mass fraction, and $\Lambda(T)$ is the cooling function (Sutherland & Dopita 1993). Results are listed in Table 5, while the cooling time profile is shown in Figure 8.

We adopted the definition of the cooling radius as the radius at which the cooling time is shorter than the age of the system. It is customary to assume the cluster's age to be equal to the look-back time at $z = 1$, since at this time many clusters appear to be relaxed: $t_{\rm age} \simeq 7.7$ Gyr.

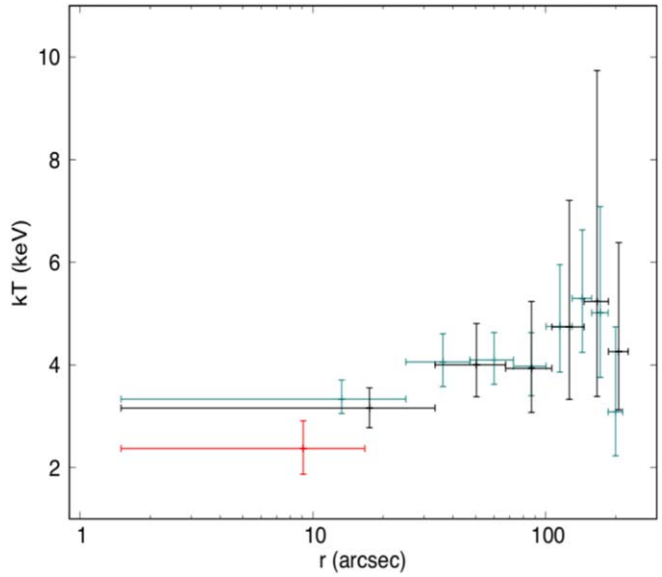

Figure 6. Projected (cyan) and deprojected (black) temperature profile of A2495. Bars in the *x*-axis represent the limits of the extraction rings, while the *y*-axis ones are the errors for the temperature values. The red point is derived from the spectral analysis described in Section 4.3.

We estimated for A2495 a cooling radius of

$$r_{\rm cool} \simeq (28 \pm 16)\ \text{arcsec} \simeq (40 \pm 23)\ \text{kpc}. \quad (6)$$

In order to determine the X-ray luminosity produced within this radius ($L_{\rm cool}$), we extracted a spectrum from a circular region with $r = r_{\rm cool}$ (excluding the central 1.″5) and fitted it with a `wabs*apec` model; Table 6 lists the results.

Therefore, the bolometric cooling luminosity is

$$L_{\rm cool} = 4.3^{+3.1}_{-3.4} \times 10^{43}\ \text{erg s}^{-1}. \quad (7)$$

The same spectrum was fitted with a `wabs*(apec +mkcflow)` model; `mkcflow` adds an isobaric multiphase component, allowing us to reproduce a cooling flow-like emission, while `apec` takes into account the background contribution. Temperature and abundance of the `apec` model were left free to vary; we bounded them to the `high temperature` and `abundance` parameter of `mkcflow`. Redshift and absorbing column density were fixed at the Galactic values (see above), while the `low temperature` parameter of `mkcflow` was fixed at ∼0.1 keV; in this way, we are assuming a standard cooling flow. The `norm` parameter of `mkcflow` provides an estimate of the mass deposition rate of the cooling flow (χ^2/dof ∼ 68/73):

$$\dot{M} < 7\ M_\odot\ \text{yr}^{-1}. \quad (8)$$

An alternative method to obtain an estimate of the mass accretion rate exploits the luminosity $L_{\rm cool}$ associated with the cooling region, assuming that it is all due to the radiation of the total gas thermal energy plus the *pdV* work done on the gas as it enters the cooling radius. These assumptions are typical of the classical cooling flow model (Fabian et al. 1994), which does not take into consideration heating produced by the central AGN,

$$\dot{M} \simeq \frac{2}{5}\frac{\mu m_p}{kT} \cdot L_{\rm cool} \simeq 52^{+38}_{-42}\ M_\odot\ \text{yr}^{-1}. \quad (9)$$

Finally, in Table 5 we list the pressure values calculated as $p = 1.83 n_e kT$, where n_e was taken from the deprojection analysis. Figure 9 shows the correspondent radial profile.

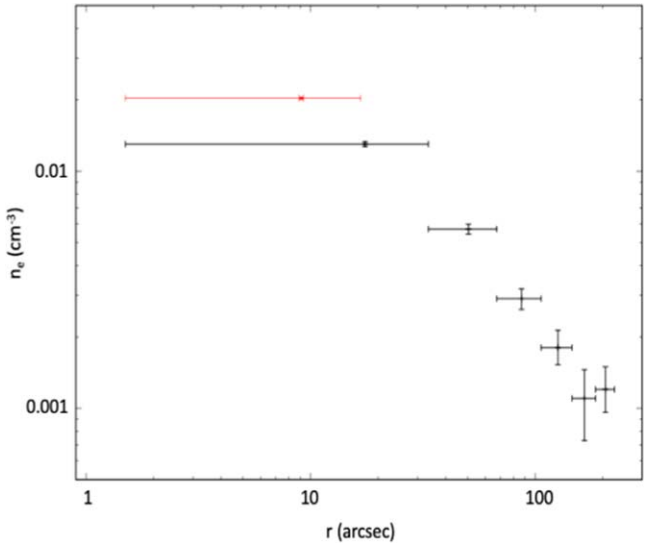

Figure 7. Density profile of A2495, obtained from the deprojection analysis. The *x*-axis bars represent the limits of the extraction rings, while the *y*-axis ones are the errors estimated for the density. The red point is derived from the spectral analysis described in Section 4.3.

Table 4
Fit Results of the Projected Radial Analysis

$r_{\rm min}$–$r_{\rm max}$ (arcsec)	Counts	kT (keV)	Z[a] ($Z_\odot$)	χ^2/dof
1.5–25.1	2230 (98.9%)	$3.35^{+0.43}_{-0.29}$	$1.04^{+0.43}_{-0.31}$	53/67
25.1–47.2	2240 (97.4%)	$4.05^{+0.55}_{-0.48}$	$0.57^{+0.41}_{-0.28}$	94/67
47.2–72.8	2002 (94.1%)	$4.09^{+0.54}_{-0.47}$	$0.46^{+0.29}_{-0.24}$	67/61
72.8–100.4	1718 (89.6%)	$3.97^{+0.65}_{-0.58}$	$0.34^{+0.32}_{-0.23}$	53/55
100.4–129.9	1513 (82.1%)	$4.75^{+1.20}_{-0.89}$	$0.36^{+0.42}_{-0.35}$	36/49
129.9–157.4	1368 (76.7%)	$5.30^{+1.34}_{-1.05}$	$0.82^{+0.81}_{-0.55}$	45/45
157.4–185.5	1151 (67.1%)	$5.01^{+2.07}_{-1.26}$	$0.44^{+0.88}_{-0.44}$	29/39
185.5–214.0	1020 (56.6%)	$3.09^{+1.65}_{-0.86}$	6.4e−02	41/35

Note. The first column shows the lower and upper limits of the extraction rings in arcseconds. The second column represents the number of source photons coming from each ring, while the percentage indicates their number compared to the total photons of the same region. Finally, in the last three columns we report the values of temperature, metallicity, and χ^2/dof, respectively.
[a] Solar abundance is estimated from the tables of Anders & Grevesse (1989).

4. Discussion

In Figure 10 we show the smoothed 0.5–2 keV image, overlaid with the 1.4 GHz contours, zoomed into the cluster center.

We highlight the presence of an offset between the BCG (R.A. = $22^{\rm h}50^{\rm m}19\overset{\rm s}{.}7$, decl. = $+10°54^{\rm m}12\overset{\rm s}{.}7$) and the X-ray peak (red circle); this suggests that there is a relative motion between them. By means of the X-ray isophotes, we estimated the centroid (bottom left panel of Figure 10, black circle), located at R.A. = $22^{\rm h}50^{\rm m}19\overset{\rm s}{.}7$, decl. = $+10°54^{\rm m}13\overset{\rm s}{.}8$. The determination was made calculating the centroid in several regions centered on the peak and with radii ranging from 50 to 200 kpc.

The offset approximately measures 4.″4 ± 1.″0, corresponding to 6.3 ± 1.4 kpc. We investigated the possibility of the presence of a point source in the position of the X-ray peak, which could bias its location, extracting a spectrum from a

Table 5
Fit Results of the Deprojection Analysis

r_{min}–r_{max} (arcsec)	Counts	kT (keV)	Z ($Z_\odot$)	$N(r)$ (10^{-4})	Electronic Density (10^{-2} cm^{-3})	Pressure (10^{-11} dyn cm^{-2})	t_{cool} (Gyr)
1.5–33.5	3143 (98.7%)	$3.16^{+0.39}_{-0.38}$	$1.09^{+0.57}_{-0.38}$	$14.3^{+2.1}_{-2.1}$	$1.30^{+0.03}_{-0.03}$	$11.8^{+1.7}_{-1.7}$	$4.0^{+0.6}_{-0.6}$
33.5–67.4	2945 (95.7%)	$4.00^{+0.80}_{-0.62}$	$0.43^{+0.39}_{-0.31}$	$21.0^{+2.5}_{-2.5}$	$0.57^{+0.03}_{-0.03}$	$6.8^{+1.7}_{-1.4}$	$10.0^{+2.5}_{-2.0}$
67.4–106.7	2430 (89%)	$3.92^{+1.30}_{-0.86}$	$0.30^{+0.50}_{-0.30}$	$17.5^{+2.8}_{-2.8}$	$0.29^{+0.03}_{-0.03}$	$3.3^{+1.4}_{-1.0}$	$20.1^{+8.7}_{-6.4}$
106.7–146.1	2042 (80.2%)	$4.79^{+2.47}_{-1.41}$	$0.32^{+0.85}_{-0.32}$	$15.2^{+2.7}_{-3.3}$	$0.18^{+0.03}_{-0.03}$	$2.6^{+1.8}_{-1.2}$	$34.0^{+22.6}_{-16.1}$
146.1–186.0	1709 (69.1%)	$5.19^{+4.50}_{-1.85}$	$1.46^{+1.47}_{-1.47}$	$8.7^{+3.7}_{-3.5}$	$0.11^{+0.04}_{-0.03}$	$1.6^{+1.9}_{-1.1}$	$61.1^{+74.3}_{-42.2}$
186.0–225.8	1384 (56.3%)	$4.27^{+2.12}_{-1.13}$	$0.16^{+0.54}_{-0.16}$	$18.1^{+2.4}_{-2.9}$	$0.12^{+0.02}_{-0.03}$	$1.6^{+1.2}_{-0.7}$	$46.9^{+32.4}_{-23.6}$

Note. The first two columns present, respectively, the limits of the annular regions and the number of source photons coming from each ring, while the percentage indicates their number compared to the total photons of the same region. The remaining columns report temperature, metallicity, normalization factor, electronic density, pressure, and cooling time. The fit gives $\chi^2/\mathrm{dof} = 394/437$.

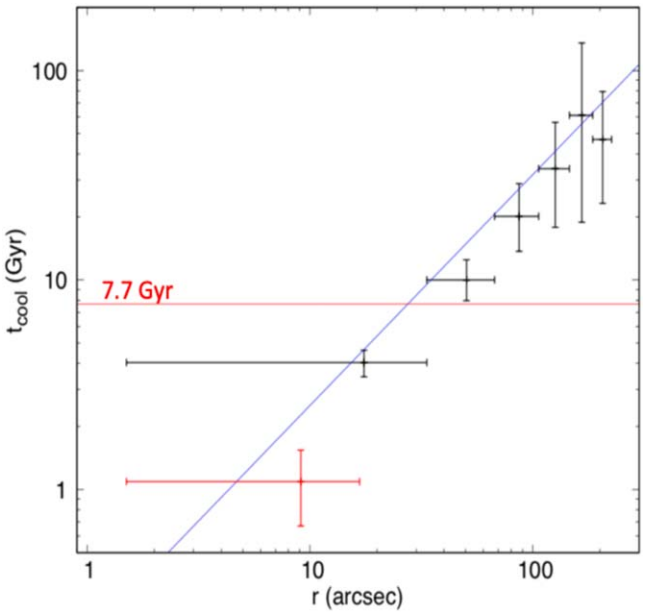

Figure 8. Cooling time profile for A2495. Each point represents the cooling time value for one of the annular regions used for the spectral extraction, and the x-axis error bars are the lower and upper limits of each ring. The red line represents $t_{age} = 7.7$ Gyr, while the blue line is the best fit of the profile: $t_{cool} = 0.199r^{1.102}$. The red point is derived from the spectral analysis described in Section 4.3.

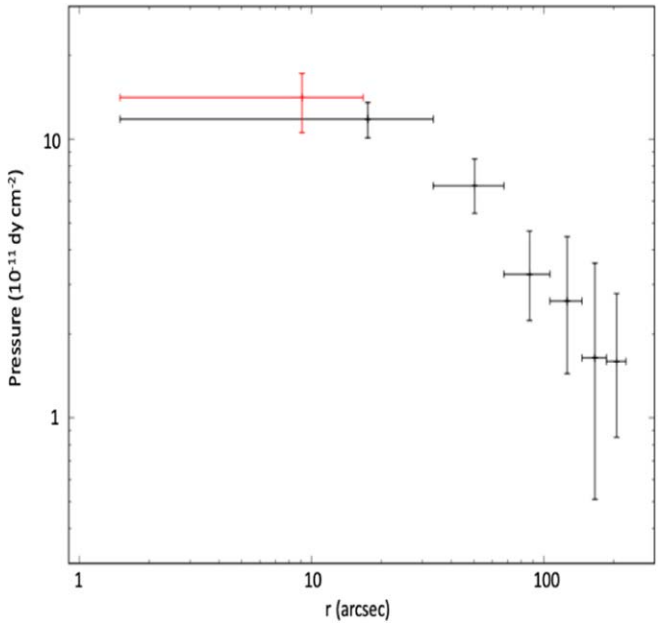

Figure 9. Pressure radial profile obtained from the deprojection analysis. The red point is derived from the spectral analysis described in Section 4.3.

$\sim 10''$ radius region centered on the peak. The radius was chosen in order to obtain enough statistics to produce a reliable fit. The spectrum was then fitted with two models: `wabs*apec` and `wabs*(apec+powerlaw)`. The `powerlaw` component, added to model the point-source emission, has two parameters: the spectral index and a normalization factor. If a point source is present, we expect a significant improvement of the fit using the second model. The first produced $\chi^2/\mathrm{dof} = 42/54$, while for the second $\chi^2/\mathrm{dof} = 40/52$. In order to determine whether the distribution improved with the addition of the `powerlaw` emission, we applied the F-stat method, obtaining $P_f = 1.3$,[10] thus indicating that the addition of a second component is not statistically significant. We then performed a search by coordinates in X-ray, optical, and infrared catalogs. However, the closest object seems to be an IR source (SSTSL2 J225019.00+105414.5) located more than 10 kpc ($\sim 7\farcs5$) away from the peak; therefore, it cannot represent its optical counterpart. We thus find no evidence of an X-ray point source at the position of the X-ray peak, and we conclude that the offset is real.

We propose that this offset could be produced by *sloshing*, an oscillation of the ICM within the cluster potential well, generated from perturbations such as, for example, minor mergers. This mechanism is usually tied to the formation of *cold fronts* (Markevitch & Vikhlinin 2007), discontinuities between the hot cluster atmosphere and a cooler region (i.e., the cooling center) that are moving with respect to each other. In this scenario, the oscillation of the ICM has displaced the X-ray peak from the cluster's center: the cooling process is not taking place on the BCG nucleus (see Section 1). However, deeper observations are necessary to test this hypothesis by means of detailed analysis of the thermodynamic properties of the galaxy cluster central regions.

4.1. Hα Emission Analysis

The detection of line-emitting nebulae in the proximity of BCGs is known to be an indicator of the presence of multiphase

[10] $p = 0.28$, corresponding to a null hypothesis probability of $P = 1 - p = 0.72$.

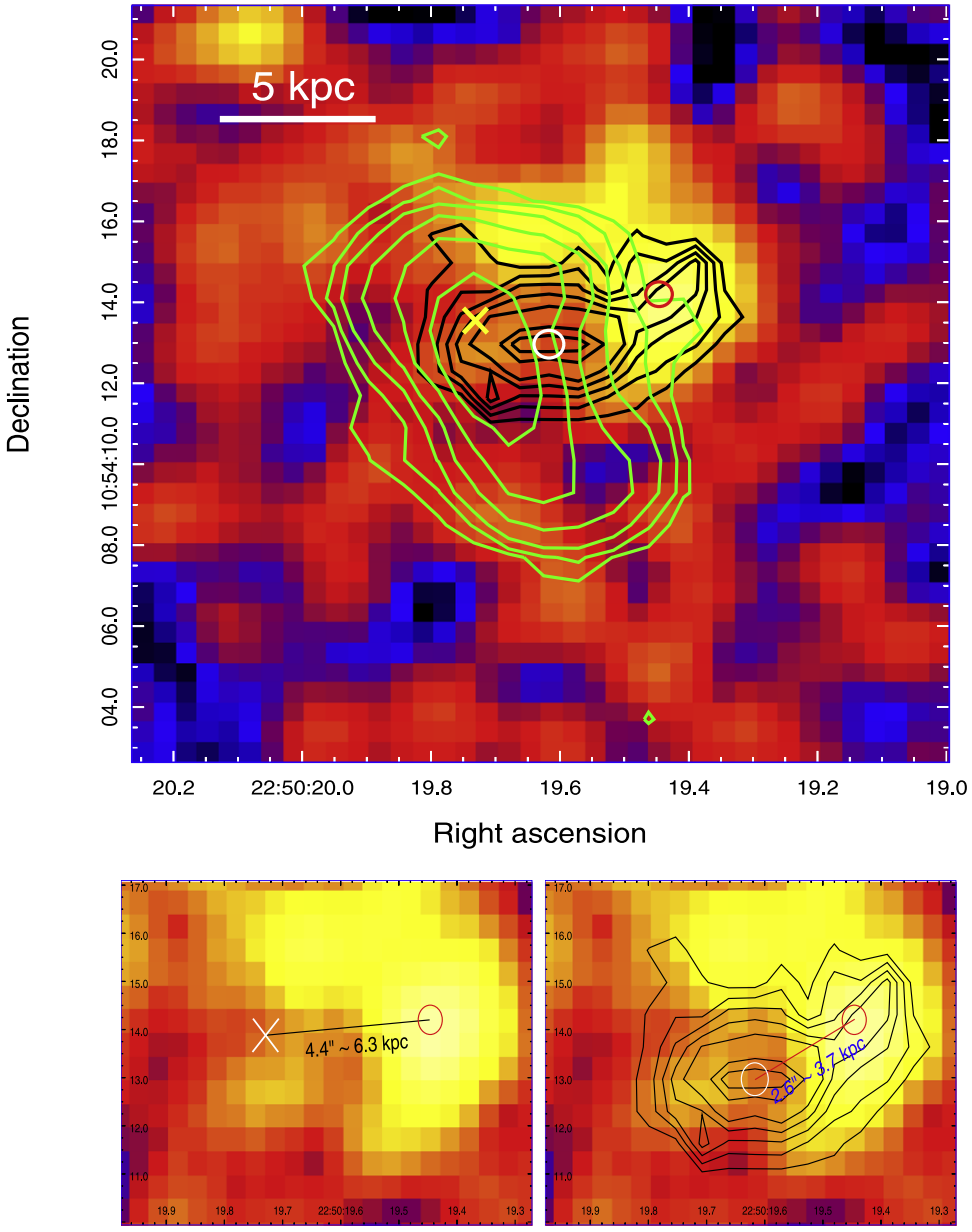

Figure 10. Top panel: 1.4 GHz (green) and Hα (black) contours overlaid on the 0.5–2 keV *Chandra* image of A2495. The red and white circles represent the X-ray and Hα peaks, respectively, while the yellow cross is the position of the X-ray centroid. Bottom left panel: offset between the emission centroid (white cross) and the X-ray peak (red circle). Bottom right panel: offset between the Hα (white circle) and the X-ray (red circle) peaks.

gas. Such structures are only found when the central entropy drops below 30 keV cm^2 or, equivalently, when $t_{\rm cool} < 5 \times 10^8$ yr (e.g., Cavagnolo et al. 2008; McNamara et al. 2016). Visible Imaging Multi-Object Spectrograph (VIMOS) observations of the Hα line emission of a sample of 73 clusters, including A2495, were presented by Hamer et al. (2016). To be consistent with the multiwavelength data shown in this work, we checked and corrected the astrometry exploiting the *HST* F606W image (see Section 4.2) and the F555W image that was used by Hamer et al. (2016) to align the VIMOS data, finding an offset of 1.″3 between the BCG centroids in them. In Figure 11 we show the astrometrically corrected Hα image.

The total luminosity is $(5.03 \pm 0.81) \times 10^{39}$ erg s^{-1}. The structure is elongated on a scale of ∼5.″6 (∼8 kpc). In Figure 10 we show the Hα emission contours (black) overlaid on the smoothed 0.5–2 keV image.

Table 6
Fit Results to the Cooling Region

Parameter	Value	Units
$r_{\rm min}$–$r_{\rm max}$	1.5–28.5	(arcsec)
Counts	2500(98.9%)	
kT	$3.29 \pm^{0.33}_{0.28}$	(keV)
Z	$0.86 \pm^{0.36}_{0.27}$	($Z_\odot$)
Flux$_{\rm Bolo}$	3.17	(10^{-12} erg s^{-1} cm^{-2})
Flux$_{2-10\ \rm keV}$	1.21	(10^{-12} erg s^{-1} cm^{-2})

Note. The χ^2/dof is 68/74.

The Hα structure stretches toward and surrounds the X-ray peak, connecting it to the BCG. The same behavior is found in other galaxy clusters (e.g., A1991, A3444, and RX J0820.9 +0752 in Bayer-Kim et al. 2002; Hamer et al. 2012; or A1111,

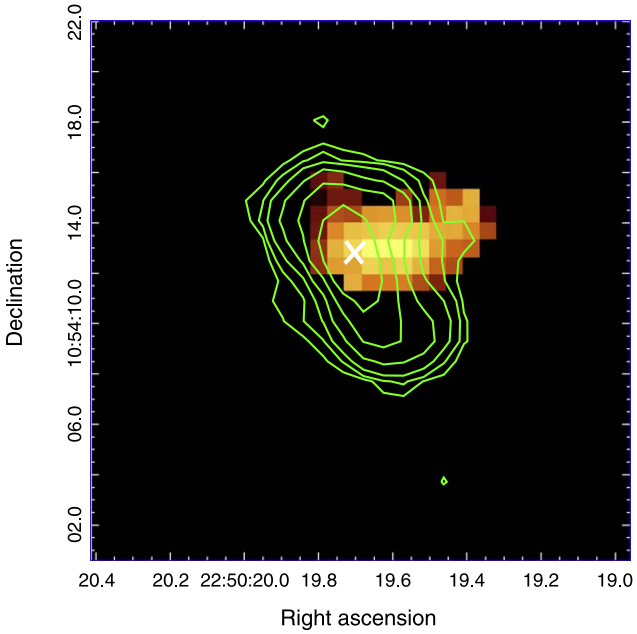

Figure 11. Hα emission structure in the inner regions of A2495 observed by VIMOS (Hamer et al. 2016). The green radio contours are the same as in Figure 10, and the white cross represents the BCG center, located in R.A. = $22^{h}50^{m}19\overset{s}{.}7$, decl. = $+10°54^{m}12\overset{s}{.}7$ (J2000). The mean seeing of the Hα image is $0\overset{''}{.}95$, and its units are in 10^{-16} erg s^{-1} cm^{-2} Å^{-1}.

A133, A2415, and others in Hamer et al. 2016), where the Hα plume either follows the X-ray peak or acts like a bridge between the peak and the BCG. This could suggest that the line emission is not produced by ionization coming from stellar radiation or from the AGN; in this scenario, in fact, one expects the emission to be associated with the BCG, rather than with the X-ray core (e.g., Crawford et al. 2005; Hamer et al. 2016). This 10^4 K gas is therefore likely connected to the cooling ICM (e.g., Bayer-Kim et al. 2002; Crawford et al. 2005; Ferland et al. 2009; Canning et al. 2012). Moreover, we note that the A2495 line emission luminosity is significantly weaker (typically of about an order of magnitude) with respect to the plumed population presented in Hamer et al. (2016); this cluster could represent a lower luminosity limit of this sample.

We also highlight the presence of a further, less pronounced ($\sim 2\overset{''}{.}6$, corresponding to 3.7 kpc) offset between the Hα and the X-ray peaks. We first checked whether it could be produced by astrometric uncertainties. The VIMOS data were obtained with a seeing of $0\overset{''}{.}95$ (from Hamer et al. 2016), while the overall 90% uncertainty circle of *Chandra* X-ray absolute position has a radius of $0\overset{''}{.}8$. The upper limit of the astrometric uncertainty is thus expected to be $\Delta x_{\rm tot} = \sqrt{\Delta x^2_{Chandra} + \Delta x^2_{\rm VIMOS}} = 1\overset{''}{.}24 \simeq 1.7$ kpc; since our offset is larger ($\sim$3.6 kpc), it is likely to be a real feature.

We argue that this offset could originate from the different hydrodynamic conditions of the ICM: the Hα emission is generated from $\sim 10^4$ K gas, $\sim 10^2$–10^3 denser than the surrounding hot ICM. Thus, hydrodynamic processes may lead to differential motion between these two phases and generate the offset. Another hypothesis is that thermal instabilities (or so-called *precipitation*) occurring in the inner regions of the cluster could have produced the 10^4 K gas in situ, following the chaotic cold accretion scenario (CCA; e.g., Gaspari et al. 2012; Voit et al. 2015, see Section 4.3).

In some cases (e.g., A1991; Hamer et al. 2012), two Hα peaks, with one being coincident with the X-ray one, are detected. As this object does not show a second, or even dominant, peak of line emission at the X-ray peak, it is possible that this represents an earlier stage of these offsets, one in which there has not yet been sufficient time for the cooled gas at the offset location to grow to a mass comparable to that already in the BCG. The plume of optical line emission shows a very clear velocity gradient (see Hamer et al. 2016 for further details), and as the ionized gas can be used as a direct tracer of the motion of the cold gas, it can be used to study the dynamics of the cold gas during the sloshing process. Following the method of Hamer et al. (2012), we estimated the dynamical offset timescale of the cold gas. The plume extends for $\sim$8 kpc from the center of the BCG ($5\overset{''}{.}6$ at 1.44 kpc arcsec^{-1}), and the gas velocity at the center of the BCG is consistent with the stellar component to within 10 km s^{-1}, indicating that the plume really extends out from the BCG and is not just a projection effect. The velocity of the gas changes smoothly and consistently along the plume, and we measured a velocity difference of $\sim$+350 km between the gas at the end of the plume and that at the center of the BCG. Thus, we measured a projected extent $D' = 8$ kpc $= 2.47 \times 10^{17}$ km and a projected velocity shift of $V' = +350$ km s^{-1}, indicating a projected timescale of $T' = D'/V' = 7.05 \times 10^{14}$ s or $\sim$22.4 Myr. To correct for the projection effects, we must know the inclination of the offset (as $T = T' \times \cos[i]/\sin[i]$). While the inclination cannot be determined from the data in hand, the most likely inclination to expect is $\sim 60°$ (Hamer et al. 2012), which would give an offset dynamical timescale of $T \sim 13$ Myr.

4.2. Optical Analysis

Deep optical images of the cluster galaxy were retrieved from the *HST* archive. We used *HST* ACS observations taken in the two wide filters F606W (V band) and F814W (I band). Images in these two filters have been instrumental in generating a dust extinction map and in the evaluation of the galaxy luminosity within the central 10 kpc. In order to estimate the dust mass in the central region, we developed a 2D galaxy model by fitting the starlight with elliptical isophotes in an iterative process with subsequent removal of sources in the field or by masking features not related to the stellar light distribution. An extinction map $A_V = -2.5 \log(I_{\rm obs}/I_{\rm model})$ (Figure 12) was generated from the observed intensity ($I_{\rm obs}$) and the intensity of the starlight model ($I_{\rm model}$).[11] To avoid the introduction of artifacts in the final map, particular care has been taken in the generation of the starlight model in the central few arcseconds, where a dust lane crosses the galactic center, making the isophote fitting process quite challenging.

The extinction map confirms that a highly absorbed dust lane crosses the galaxy center, while a large wavy filamentary structure extends to the west for about $4''$. Additional knots of highly absorbed dust are apparent in the central kiloparsec of the galaxy. Although the peak of the warm ionized gas does not correspond to the galactic center or any other location of high extinction, the lower ridge of the Hα emission seems to be associated with dust absorption revealed in the filamentary structure.

[11] We also tried an alternative method, performing a ratio of the F606W and F814W images, in order to avoid the dustiest regions in the galaxy, which could affect the starlight fitting process. However, we only found a difference of $\sim$20% between the results of the two methods.

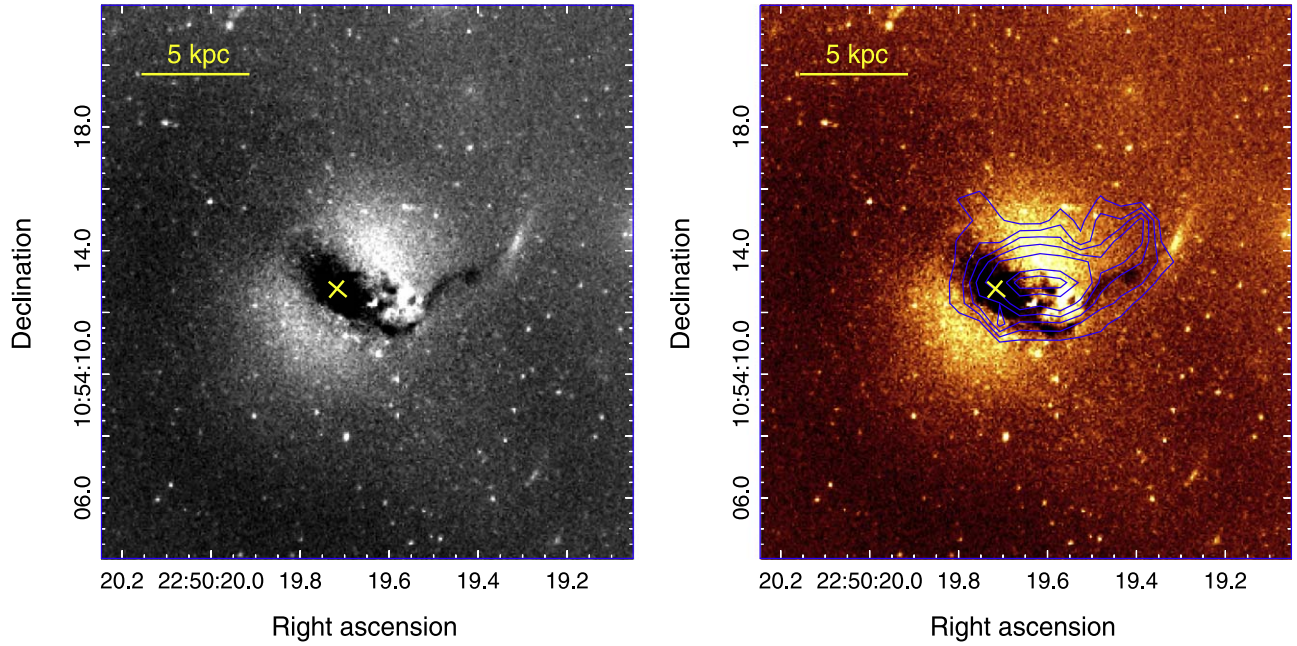

Figure 12. Left panel: dust extinction map of the BCG and core of A2495, obtained from the F606W *HST* image. Dust in absorption, seen as a filamentary structure, encircles the inner region of the galaxy and stretches toward the outskirts. The yellow cross represents the BCG optical center. Right panel: Hα contours overlaid on the dust extinction map. The two structures are cospatial.

Dust structures are common in BCGs. Van Dokkum & Franx (1995) detected dust in 50% of the galaxies included in their sample of 64 objects; Laine et al. (2003) found signs of dust absorption in 38% of 81 BCGs, classifying them, according to their morphology, into nuclear dust disk, filaments, patchy dust, dust rings, and dust spirals (see Section 3.2 and Figure 3 of Laine et al. 2003 for further details). The structure in A2495 seems to fall into the second class, looking like a classic dust filament. The BCG of this cluster was also part of the large *Spitzer* dust survey presented by Quillen et al. (2008) and discussed in O'Dea et al. (2008); these studies highlighted that dust in A2495 does not show a particularly remarkable mid-IR continuum and is not detected at 70 μm, likely suggesting that the star formation does not significantly heat the dust as it is, instead, seen in other systems (see Quillen et al. 2008 for more details).

From the extinction map we calculated the total dust mass in the central 7 kpc under some basic assumptions for the grain size distribution and composition. The approach and relative calculations are outlined in Goudfrooij et al. (1994); here we assume dust extinction properties similar to what is observed in the Milky Way. We used a grain size distribution proportional to $a^{-3.5}$ (where a is the grain radius; Mathis et al. 1977; Goudfrooij et al. 1994) and a mixture of graphite and silicate (equal absorption from those) with a specific grain mass density of $3\,\mathrm{g\,cm^{-3}}$. Lower and upper limits for the grain size distribution were set to $a_- = 0.005$ μm and $a_+ = 0.22$ μm (Draine & Lee 1984). The filamentary structure was divided into five sectors, as shown in Figure 13.

The total dust mass accounted in all the filamentary structures in the central 7 kpc is $1.7 \times 10^5\ M_\odot$. The reported mass should be regarded as a lower limit, considering that the method used in generating the extinction map would mask a centrally symmetric diffuse dust component, if present. Given the uncertainties in the generation of an accurate galaxy model at the galactic center and the statistical error, we estimate a 30% uncertainty in the reported dust mass. We remark that the optically detected dust likely underestimates the total dust content (see, e.g., Temi et al. 2004, for a study of dust in a sample of elliptical galaxies).

Assuming a dust/gas ratio of $M_{\rm dust}/M_{\rm gas} \sim 1/100$ (e.g., Edge et al. 2010), we expect for A2495 a minimum cold gas mass within the central 7 kpc of $\sim 2 \times 10^7\ M_\odot$ (again, with a 30% uncertainty). We note that the mass of the Hα-emitting gas within the same region (assuming that it is optically thin and in pressure equilibrium with the local ICM) is

$$M_{\rm H\alpha} \simeq L_{\rm H\alpha} \frac{\mu m_p}{n_{\rm H\alpha}\, \epsilon_{\rm H\alpha}}, \tag{10}$$

where $L_{\rm H\alpha}$ is that reported in Section 4.1 and $\epsilon_{\rm H\alpha} \sim 3.3 \times 10^{-25}$ erg cm^3 s^{-1} is the Hα line emissivity; $n_{\rm H\alpha}$ is obtained assuming

$$n_{\rm H\alpha}\, T_{\rm H\alpha} \simeq n_{\rm ICM}\, T_{\rm ICM}, \tag{11}$$

where $T_{\rm H\alpha} \sim 10^4$ K, $T_{\rm ICM}$ is the first value reported in Table 8 (since the Hα structure is located within the central 7 kpc), and $n_{\rm ICM} \sim 1.83 n_e$. Again, n_e can be retrieved from Table 8. We thus obtain $M_{\rm H\alpha} \sim 10^5 \pm 10^4\ M_\odot$.

The Hα mass can account for just a negligible fraction of the total cold gas mass estimated above: a significant amount is still missing. We speculate that colder, likely molecular gas is present in the central regions of A2495. This is supported by the correlation between the Hα luminosity and the molecular mass (Edge 2001; Pulido et al. 2018), from which we obtain $M_{\rm mol} \sim 10^9\ M_\odot$. The contrast with the estimate determined from the dust/gas ratio is only apparent: the latter takes into account the dust mass within the central 7 kpc of the BCG and constitutes, per se, a lower limit (see above). Cold molecular gas could also lie offset from the BCG, as observed in other systems where evidence for CO line emission coincident with the offset X-ray peak was detected (e.g., Hamer et al. 2012).

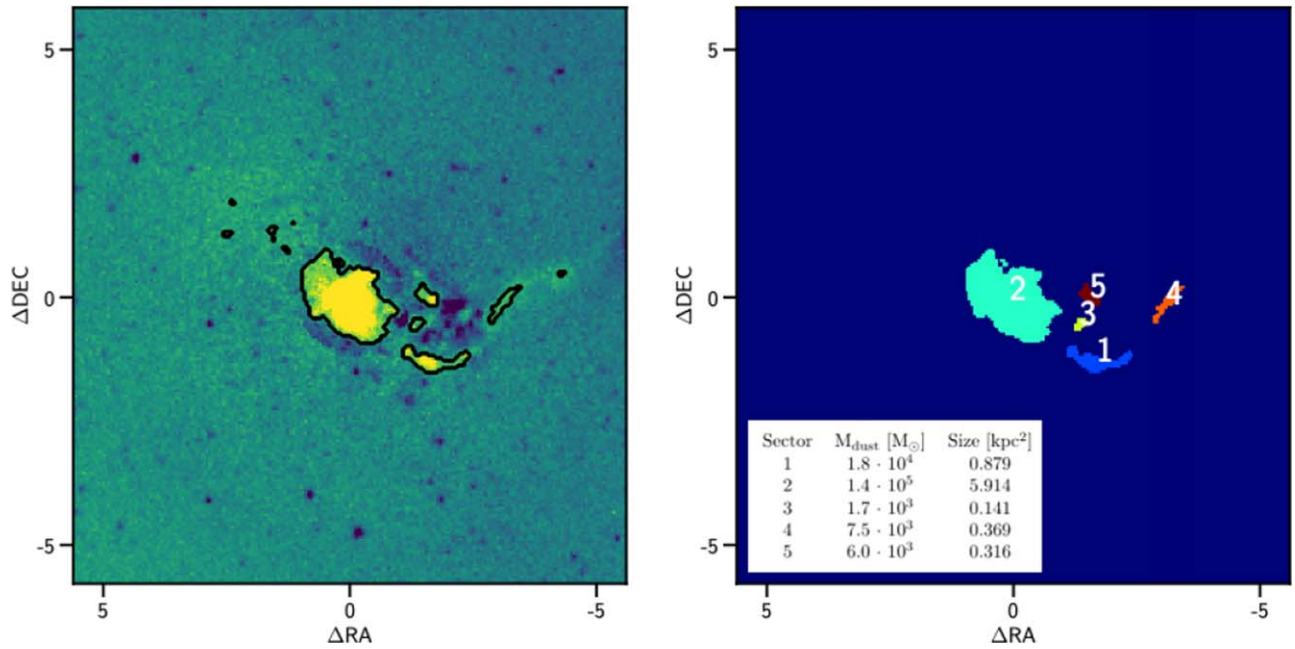

Figure 13. Sectors in which the dust mass estimation was performed. The table shows the dust mass values and the size for each sector. ΔR.A. = 0, Δdecl. = 0 corresponds to the BCG optical center (see Section 2.1).

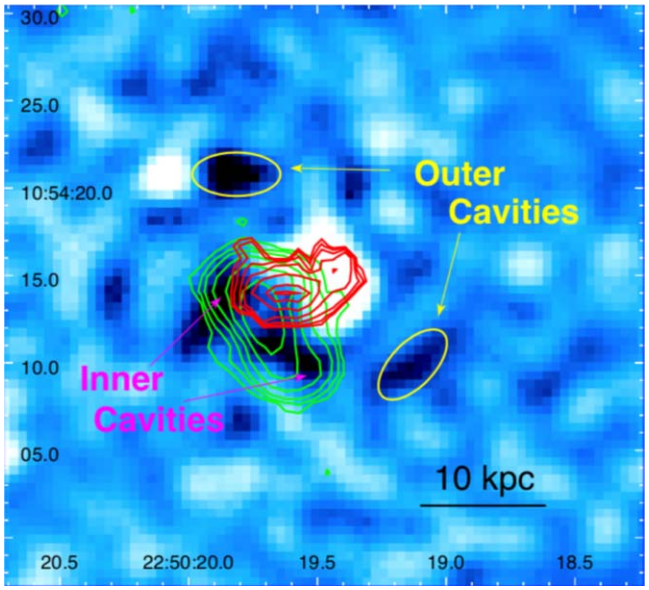

Figure 14. Residual image showing the two cavity systems located in A2495. The first pair is coincident with the radio lobes, while the second is symmetrical with respect to the X-ray peak region. The Hα contours are overlaid in red, while the green contours are the same as in Figure 10.

4.3. Does Sloshing Regulate the Generation of Multiple Cavity Systems?

We investigated the presence of cavities in A2495 by considering a residual image obtained by subtracting a 2D β-model from the 0.5–2 keV image. The result is shown in Figure 14.

We notice an X-ray blob surrounding the peak region and four ICM depressions (two pairs), corresponding to ∼30% (at 90% confidence level) surface brightness deficits. Although we are aware of the limitations of our snapshot exposure, we notice that their shape and position, symmetrical with respect to the BCG for the first pair and to the X-ray peak for the second one (see Figure 14), suggest that they could be real structures. In the following analysis and discussion, we assume them as cavities. However, it is possible that the poor statistic could have led to the production of artifacts; the reader shall thus be warned about the significance of these depressions. Deeper observations are therefore required to confirm their significance.

Table 7
Properties of the Two-cavity Systems of A2495

Cavity	a (kpc)	b (kpc)	V (kpc^3)	R (kpc)
Inner	6.8	2.9	70.3	4.9
Outer	8.0	4.9	164.0	11.9

Note. Here a and b are the major and minor axis, respectively, V is the volume (estimated assuming an oblate ellipsoidal shape), and R is their distance from the BCG center.

The first pair seems to be coincident with the radio galaxy lobes, while the second pair is centered on, and falls on opposite sides of, the X-ray excess. Hereafter, we will refer to them as, respectively, *inner* and *outer* cavities. We also assume that cavities belonging to the same pair are characterized by the same elliptical shape and dimensions. Table 7 lists their properties (a refers to the major axis, b to the minor one).

Following the method described in Bîrzan et al. (2004), the cavity power can be estimated as

$$P_{\rm cav} = \frac{E_{\rm cav}}{t_{\rm cav}} = \frac{4pV}{t_{\rm cav}}, \quad (12)$$

where $t_{\rm cav}$ is the age of the cavity. In order to obtain an estimate of the temperature closer to the cavities' region, we performed a deprojection analysis with annular regions containing a minimum of 1500 counts; in fact, lowering the counts' lower limit makes the ring's radius smaller, bringing to a more

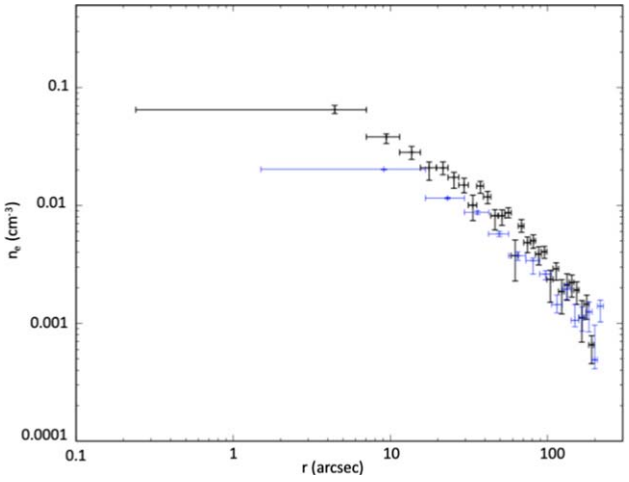

Figure 15. The black data are the results obtained from the double β-model fit on the surface brightness profile, while the blue data are the results obtained from the spectral analysis described above.

localized estimate of the thermodynamical properties, albeit with larger uncertainties. However, we note that since we are close to the X-ray peak, the photon statistics remains high enough to obtain a good fit. We fitted a `project*wabs*apec` model and obtained the kT value; results for the inner region, which corresponds to the radius we are interested in, are represented with a red circle in Figures 6–9.

Density was, instead, obtained exploiting the surface brightness profile shown in Figure 5. In fact, fitting a double β-model on it (for details of this method, see Ettori et al. 2002) allows us to obtain an estimate for the density values for smaller radii with respect to the spectral analysis performed above. Results are shown in Figure 15.

Since the two cavity systems lie at, respectively, ∼4.9 and ∼11.9 kpc from the cluster center (see Table 7), we will make use of the first two density values: the first will be used for the inner cavities, the second for the outer ones. The kT estimated above will instead be exploited for both systems, since the current statistics does not allow us to provide more localized values. In Table 8 we finally report temperatures, densities, and pressures used for the estimate of the cavities' properties.

The cavity age was calculated as $t_{\rm cav} = R/v$, where R is that defined in Table 7, while v is the cavity velocity. In this work, we will consider the sound and the buoyancy velocity.

The latter is defined as

$$v_{\rm buoy} = \sqrt{\frac{2gV}{CA}}, \tag{13}$$

where $C \simeq 0.75$ represents the drag coefficient, V and A are the volume and area of each cavity, respectively, and g is the gravitational acceleration.

We estimated the latter by making use of the galaxy luminosity profile (see the Appendix) and of a simple model for the dark matter halo. We adopted a stellar $M/L_V \sim 4$, appropriate for an old stellar population with roughly solar abundance (es. Maraston 2005). The resulting stellar masses within the region of the inner and outer cavities are $M_{\rm BCG}(r < 4.9\ {\rm kpc}) \sim 8.8 \times 10^{10}\ M_\odot$ and $M_{\rm BCG}(r < 11.9\ {\rm kpc}) \sim 2.3 \times 10^{11}\ M_\odot$, respectively. Given the uncertainty on the mass-to-light ratio, we adopted for these values a 30% error.

Table 8
Thermodynamical Properties of the Inner Regions Obtained from the Deprojection Analysis with 1500 Counts (χ^2/dof ∼ 450/441) and from the Fit of the Surface Brightness Profile

$r_{\rm min}$–$r_{\rm max}$ (arcsec)	kT[a] (keV)	n_e[b] (10^{-2} cm^{-3})	p (10^{-11} dyn cm^{-2})
0.2–7	$2.37^{+0.64}_{-0.55}$	$6.49^{+0.59}_{-0.45}$	$45.0^{+14.3}_{-12.6}$
7–11.5	$2.37^{+0.64}_{-0.55}$	$3.83^{+0.22}_{-0.47}$	$26.6^{+7.6}_{-8.9}$

Notes. The results of the spectral analysis are represented with red circles in Figures 6–9.
[a] Obtained from the spectral analysis.
[b] Obtained from the surface brightness profile.

We estimated the dark matter contribution by assuming a NFW halo (Navarro et al. 1996) of mass $M_{\rm NFW} = 3.8 \times 10^{14}\ M_\odot$, estimated from the M–T relation of Finoguenov et al. (2001), and a concentration $c = 4.65$ (Prada et al. 2012; Merten et al. 2015). We note that the assumed mass is somewhat larger than the richness-based estimate by Andreon (2016) (∼$1.6 \times 10^{14} M_\odot$). On the other hand, it is consistent with the hydrostatic mass (e.g., Gitti et al. 2012) determined exploiting the β-model (presented in Section 3.2.1), which returns $M \sim 3.2 \times 10^{14}\ M_\odot$. However, the conclusions for the cavity dynamics discussed below are quite insensitive to the precise values of $M_{\rm NFW}$ and c. This model estimates dark masses of $M_{\rm DM}(r < 4.9\ {\rm kpc}) = 3.3 \times 10^{10}\ M_\odot$ and $M_{\rm DM}(r < 11.9\ {\rm kpc}) = 1.8 \times 10^{11}\ M_\odot$.

We therefore obtain a total mass within the central 4.9 kpc of $M_{\rm tot}(r < 4.9\ {\rm kpc}) \sim 1.2 \times 10^{11}\ M_\odot$, while $M_{\rm tot}$ ($r <$ 11.9 kpc) $\sim 4.1 \times 10^{11}\ M_\odot$. Results of the cavity analysis are listed in Table 9.

It is plausible that we are observing two different generations of cavities; the outer ones are older, while the inners probably still lie in the same regions in which they formed. From this, we can infer that some process is probably switching the radio galaxy on and off: after the first generation forms, the AGN turns off and the cavities start to rise in the cluster atmosphere by buoyancy. Eventually, the AGN turns on again and another generation can be formed.

Following the CCA, cold gas could originate if thermal instabilities ensue (e.g., Gaspari et al. 2012). According to Voit et al. (2015), this is likely to happen when $t_{\rm cool}/t_{\rm ff} \leqslant$ 10–20, where $t_{\rm ff} = \sqrt{2R^3/GM}$ is the *freefall time*. We note that, with the cooling time profile in Figure 8 and the masses estimated above, this condition is not verified in A2495. However, McNamara et al. (2016) propose that the $t_{\rm cool}/t_{\rm ff}$ ratio could be almost entirely governed by the cooling time. In both these interpretations, the cold gas could then accrete onto the SMBH efficiently and activate it.

We propose that in A2495 the sloshing process mentioned above could also play a part in the feedback cycle. When the cooler region approaches the BCG, the AGN begins to accrete and turns on, producing the first generation of cavities. Subsequently, because of sloshing, the accreting material diminishes and the SMBH is switched off. The oscillation could, at a later time, make the process repeat. This would produce different generations of cavities.

In order to investigate this scenario, we determined the freefall time of the cooler region and compared it with the age difference of the two cavity generations, estimated with both

Table 9
Cavity Velocity, Age, and Power Estimated with Both Methods Described in the Text

	Sound Velocity			Buoyancy Velocity		
	c_s (km s^{-1})	Age (Myr)	P_{cav} (10^{42} erg s^{-1})	v (km s^{-1})	Age (Myr)	P_{cav} (10^{42} erg s^{-1})
Inner	790^{+105}_{-83}	$6.0^{+0.8}_{-0.6}$	$18.3^{+7.5}_{-6.6}$	259 ± 58	18 ± 4	$6.0^{+2.3}_{-2.1}$
Outer	790^{+105}_{-83}	$14.4^{+1.7}_{-1.5}$	$10.4^{+3.7}_{-4.1}$	214 ± 42	53 ± 11	$2.8^{+0.9}_{-1.1}$

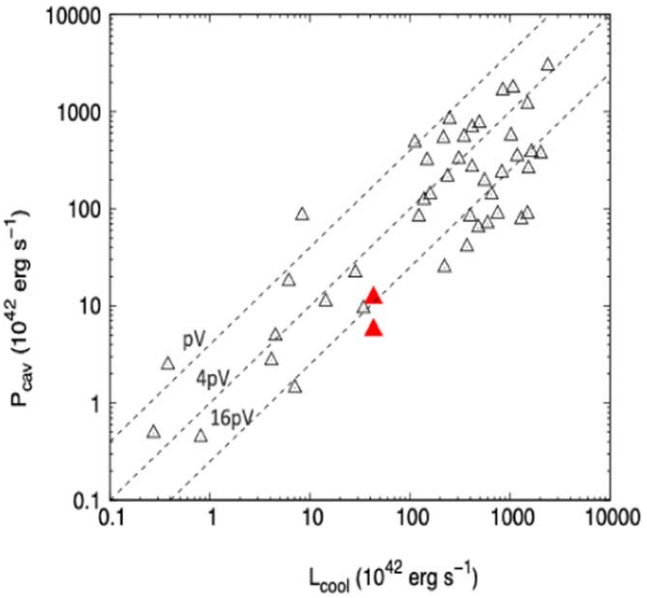

Figure 16. Black triangles represent the data from Bîrzan et al. (2017), while in red are the values for the two putative cavity systems considered in this work.

methods seen above. We obtained

$$\begin{cases} t_{\rm ff} \simeq 15.4 \pm 5.7 \text{ Myr} \\ \Delta t_{\rm cav}^{\rm sound} \simeq 8.4\ ^{+2.1}_{-1.8} \text{ Myr} \\ \Delta t_{\rm cav}^{\rm buoy} \simeq 35 \pm 12 \text{ Myr}. \end{cases} \quad (14)$$

We thus estimate $\Delta t_{\rm cav} \simeq t_{\rm ff}$: the age difference between cavities reflects the timescale needed for the cooling region to move toward the BCG and activate the AGN. This is also consistent with the dynamical timescale obtained in Section 4.1, which provides an alternative estimate for the offset lifetime.

Future works, exploiting deeper observations, will likely be able to confirm or disprove our hypothesis.

4.4. Can Offset Cooling Affect the Feedback Process?

As we showed in the previous sections, the existing data suggest that cooling deposits gas away from the BCG nucleus, so it cannot fuel the AGN. Therefore, we aim at investigating whether this can break the feeding-feedback cycle in A2495, or if the AGN activation cycle is driven by the periodicity of the gas sloshing motions.

We thus compared the power of the two putative cavity systems with the data available from samples of these structures (Bîrzan et al. 2017). The result is presented in Figure 16, with the x-axis representing the luminosity emitted within the cooling radius (estimated in Section 3.2.2). For the cavity power, we used the values obtained from the buoyancy velocity, for consistency with the work cited above.

The values we estimated for A2495 are in good agreement with the global scatter of the observed relation. Therefore, we can argue that offset cooling seems to not break the feedback cycle, despite the evidence that cooling is not currently depositing gas into the BCG core, where it can feed the AGN. Nevertheless, as we argued above, offsets probably still play a significant role in in the cycle regularization.

5. Conclusions

We carried out a thorough analysis of the X-ray and radio properties of A2495, by means of new observations requested with the purpose of performing a combined EVLA/*Chandra* study of this cool-core galaxy cluster. We also discussed Hα emission data from Hamer et al. (2016) and exploited optical images retrieved from the *HST* archive. Our main results can be summarized as follows:

1. The radio analysis at 1.4 and 5 GHz presented a small ($\sim$13–15 kpc) FR I radio galaxy with $L(1.4\text{GHz}) \sim 2 \times 10^{23}$ W Hz^{-1} and no apparent diffuse emission. This places A2495 as having the least radio powerful BCG among the 13 BCS objects that meet our selection criteria. The spectral index map highlighted a very steep synchrotron spectrum ($\alpha \simeq 1.35$), suggesting the presence of an old electronic population.
2. The X-ray study allowed us, through a deprojection analysis, to estimate the cooling radius of the cluster ($\sim$28″, corresponding to 40 kpc) and its luminosity (4.3×10^{43} erg s^{-1}). Furthermore, we determined the cooling time, the density, and the pressure radial profiles, finding $t_{\rm cool} < 1$ Gyr inside $\sim$20 kpc.
3. The multiwavelength analysis showed two significant offsets, one of $\sim$6 kpc between the emission centroid and the X-ray peak, and the other one ($\sim$4 kpc) between the X-ray and the Hα peaks. We propose that the first could be produced by sloshing of the ICM, while the second still remains unexplained and is worthy of more investigations. The line-emitting plume connects the X-ray core emission to the BCG, suggesting that the origin of the 10^4 K gas could be linked to the cooling ICM. We found two putative cavity systems, the inner one with $t_{\rm age} \sim 18$ Myr and $P_{\rm cav} \sim 1.2 \times 10^{43}$ erg s^{-1}, while for the outer one $t_{\rm age} \sim 53$ Myr and $P_{\rm cav} \sim 5.6 \times 10^{42}$ erg s^{-1}. Their age difference is consistent with the freefall time of the central cooling gas and with the offset dynamical timescale estimated from the line-emitting gas; we thus suggest that the same sloshing motions could switch the AGN on and off, forming different generations of cavities.
4. Exploiting *HST* images, we located a dust lane crossing the BCG core in the north–south direction and a $\sim$4″ filament extending west; we determined the dust mass within the central 7 kpc, finding $\sim 1.7 \times 10^5$ $M_\odot$. We estimated in this region a lower limit for the total gas mass of $\sim 10^7$ $M_\odot$ and argued that, since the Hα structure

cannot entirely account for it, a significant fraction is still missing. We propose that this fraction consists primary of molecular gas; the $L_{H\alpha}$–M_{mol} correlation supports this hypothesis, providing an estimate of $M_{mol} \sim 10^9\ M_\odot$.

5. Finally, we proved that the offset cooling we found does not break the feedback cycle, since the cavity power values for A2495 with respect to the cooling luminosity are in agreement, within the scatter, with the observed P_{cav}–L_{cool} correlation.

Deeper multiwavelength observations (e.g., *Chandra*, ALMA) will be required in order to better investigate the hypothesis we made in this work. A similar combined analysis of the other 12 BCS clusters that meet our selection criteria, and that apparently show similar features, will provide a better understanding of these dynamically active environments.

We thank the referee for the careful reading of the manuscript and thoughtful comments and suggestions, which have significantly improved the presentation of our results. E.O'S. gratefully acknowledges funding support for this work provided by the National Aeronautics and Space Administration (NASA) through *Chandra* award No. GO8-19112A issued by the Chandra X-ray Center, which is operated by the Smithsonian Astrophysical Observatory for and on behalf of the National Aeronautics Space Administration under contract NAS8-03060.

Appendix

We exploited deep *HST V*-band observations to derive the luminosity profile and structural parameters of the galaxy. The results obtained from this analysis have been used in Section 4.3 to derive an estimate of the BCG mass. As discussed by several authors (e.g., Schombert 1987; Graham et al. 2005), BCGs have a flux excess at large radii with respect to the $R^{1/4}$ de Vaucouleurs law often used to fit the light profile in ellipticals. Here we follow the approach outlined by Donzelli et al. (2011), where the luminosity profile fitting procedure uses a combination of a Sérsic and an exponential function to reproduce the inner and outer components of the surface brightness profile. Briefly, the isophote fitting procedure ELLIPSE, within the IRAF STSDAS package, was used to extract the luminosity profile from the *V*-band image. Each function used in the light profile fitting process provides a set of photometric parameters: from the Sérsic model we derived the surface brightness μ_e at $r = r_e$ (the half-light radius) and the Sérsic index n; the exponential model is characterized by μ_0 and r_0, which respectively represent the surface brightness at the center and the length scale. Finally, the total luminosity was computed by separately integrating the two fitting models characterized by the photometric parameters.

As a result of the fitting procedure, we obtained $r_e = 11.9$ kpc and $r_0 = 43.7$ kpc from the Sérsic (best-fit index = 1.89) and exponential models, respectively. It is worth noting that a large fraction of the total luminosity is contributed by the exponential model component, implying that a single de Vaucouleurs or Sérsic component could not reproduce the faint end of the light profile. The computed total luminosity is $L_V = 4.1 \times 10^{11}\ L_\odot$, which includes a galactic extinction correction. In order to evaluate the galaxy mass at the location of inner and outer cavities (see Section 4.3), we have computed the luminosities of $L_V(r < 4.9\ \text{kpc}) = 2.2 \times 10^{10}\ L_\odot$ and $L_V(r < 11.9\ \text{kpc}) = 5.8 \times 10^{10}\ L_\odot$.

ORCID iDs

M. Gitti https://orcid.org/0000-0002-0843-3009
P. Temi https://orcid.org/0000-0002-8341-342X
E. O'Sullivan https://orcid.org/0000-0002-5671-6900
F. Gastaldello https://orcid.org/0000-0002-9112-0184

References

Anders, E., & Grevesse, N. 1989, GeCoA, 53, 197
Andreon, S. 2016, A&A, 587, A158
Bayer-Kim, C. M., Crawford, C. S., Allen, S. W., Edge, A. C., & Fabian, A. C. 2002, MNRAS, 337, 938
Bîrzan, L., Rafferty, D. A., Brüggen, M., & Intema, H. T. 2017, MNRAS, 471, 1766
Bîrzan, L., Rafferty, D. A., McNamara, B. R., Wise, M. W., & Nulsen, P. E. J. 2004, ApJ, 607, 800
Canning, R. E. A., Russell, H. R., Hatch, N. A., et al. 2012, MNRAS, 420, 2956
Cavagnolo, K. W., Donahue, M., Voit, G. M., & Sun, M. 2008, ApJL, 683, L107
Cavaliere, A., & Fusco-Femiano, R. 1976, A&A, 49, 137
Crawford, C. S., Allen, S. W., Ebeling, H., Edge, A. C., & Fabian, A. C. 1999, MNRAS, 306, 857
Crawford, C. S., Sanders, J. S., & Fabian, A. C. 2005, MNRAS, 361, 17
Cui, W., Power, C., Biffi, V., et al. 2016, MNRAS, 456, 2566
Donzelli, C. J., Muriel, H., & Madrid, J. P. 2011, ApJS, 195, 15
Draine, B. T., & Lee, H. M. 1984, ApJ, 285, 89
Dutson, K. L., Edge, A. C., Hinton, J. A., et al. 2014, MNRAS, 442, 2048
Ebeling, H., Edge, A. C., Bohringer, H., et al. 1998, MNRAS, 301, 881
Edge, A. C. 2001, MNRAS, 328, 762
Edge, A. C., Oonk, J. B. R., Mittal, R., et al. 2010, A&A, 518, L47
Ettori, S., De Grandi, S., & Molendi, S. 2002, A&A, 391, 841
Fabian, A. C. 2012, ARA&A, 50, 455
Fabian, A. C., Canizares, C. R., & Boehringer, H. 1994, ApJ, 425, 40
Fabian, A. C., Sanders, J. S., Taylor, G. B., et al. 2006, MNRAS, 366, 417
Feretti, L., & Giovannini, G. 2008, LNP, 740, 143
Ferland, G. J., Fabian, A. C., Hatch, N. A., et al. 2009, MNRAS, 392, 1475
Finoguenov, A., Arnaud, M., & David, L. P. 2001, ApJ, 555, 191
Gaspari, M., McDonald, M., Hamer, S. L., et al. 2018, ApJ, 854, 167
Gaspari, M., Melioli, C., Brighenti, F., & D'Ercole, A. 2011, MNRAS, 411, 349
Gaspari, M., Ruszkowski, M., & Oh, S. P. 2013, MNRAS, 432, 3401
Gaspari, M., Ruszkowski, M., & Sharma, P. 2012, ApJ, 746, 94
Gitti, M., Brighenti, F., & McNamara, B. R. 2012, AdAst, 2012, 950641
Goudfrooij, P., de Jong, T., Hansen, L., & Norgaard-Nielsen, H. U. 1994, MNRAS, 271, 833
Graham, A. W., Driver, S. P., Petrosian, V., et al. 2005, AJ, 130, 1535
Hamer, S. L., Edge, A. C., Swinbank, A. M., et al. 2012, MNRAS, 421, 3409
Hamer, S. L., Edge, A. C., Swinbank, A. M., et al. 2016, MNRAS, 460, 1758
Heckman, T. M., Baum, S. A., van Breugel, W. J. M., & McCarthy, P. 1989, ApJ, 338, 48
Hogan, M. T., Edge, A. C., Geach, J. E., et al. 2015a, MNRAS, 453, 1223
Hogan, M. T., Edge, A. C., Hlavacek-Larrondo, J., et al. 2015b, MNRAS, 453, 1201
Hogan, M. T., McNamara, B. R., Pulido, F. A., et al. 2017, ApJ, 851, 66
Hudson, D. S., Mittal, R., Reiprich, T. H., et al. 2010, A&A, 513, A37
Kalberla, P. M. W., Burton, W. B., Hartmann, D., et al. 2005, A&A, 440, 775
Katayama, H., Hayashida, K., Takahara, F., & Fujita, Y. 2003, ApJ, 585, 687
Laine, S., van der Marel, R. P., Lauer, T. R., et al. 2003, AJ, 125, 478
LaRoque, S. J., Bonamente, M., Carlstrom, J. E., et al. 2006, ApJ, 652, 917
Mann, A. W., & Ebeling, H. 2012, MNRAS, 420, 2120
Maraston, C. 2005, MNRAS, 362, 799
Markevitch, M., & Vikhlinin, A. 2007, PhR, 443, 1
Mathis, J. S., Rumpl, W., & Nordsieck, K. H. 1977, ApJ, 217, 425
McDonald, M., Swinbank, M., Edge, A. C., et al. 2014, ApJ, 784, 18
McDonald, M., Veilleux, S., Rupke, D. S. N., & Mushotzky, R. 2010, ApJ, 721, 1262
McNamara, B. R., & Nulsen, P. E. J. 2007, ARA&A, 45, 117
McNamara, B. R., Russell, H. R., Nulsen, P. E. J., et al. 2016, ApJ, 830, 79
McNamara, B. R., Wise, M., Nulsen, P. E. J., et al. 2000, ApJL, 534, L135
Merten, J., Meneghetti, M., Postman, M., et al. 2015, ApJ, 806, 4

Mittal, R., Hudson, D. S., Reiprich, T. H., & Clarke, T. 2009, A&A, 501, 835
Mohr, J. J., Mathiesen, B., & Evrard, A. E. 1999, ApJ, 517, 627
Navarro, J. F., Frenk, C. S., & White, S. D. M. 1996, ApJ, 462, 563
O'Dea, C. P., Baum, S. A., Privon, G., et al. 2008, ApJ, 681, 1035
Owen, F. N., & Ledlow, M. J. 1997, ApJS, 108, 41
Patel, P., Maddox, S., Pearce, F. R., Aragón-Salamanca, A., & Conway, E. 2006, MNRAS, 370, 851
Peterson, J. R., & Fabian, A. C. 2006, PhR, 427, 1
Prada, F., Klypin, A. A., Cuesta, A. J., Betancort-Rijo, J. E., & Primack, J. 2012, MNRAS, 423, 3018
Pulido, F. A., McNamara, B. R., Edge, A. C., et al. 2018, ApJ, 853, 177
Quillen, A. C., Zufelt, N., Park, J., et al. 2008, ApJS, 176, 39
Rafferty, D. A., McNamara, B. R., Nulsen, P. E. J., & Wise, M. W. 2006, ApJ, 652, 216
Rau, U., & Cornwell, T. J. 2011, A&A, 532, A71
Rines, K. J., Geller, M. J., Diaferio, A., & Hwang, H. S. 2016, ApJ, 819, 63
Rossetti, M., Gastaldello, F., Eckert, D., et al. 2017, MNRAS, 468, 1917
Rossetti, M., Gastaldello, F., Ferioli, G., et al. 2016, MNRAS, 457, 4515
Russell, H. R., McNamara, B. R., Fabian, A. C., et al. 2019, MNRAS, 490, 3025
Sanderson, A. J. R., Edge, A. C., & Smith, G. P. 2009, MNRAS, 398, 1698
Schombert, J. M. 1987, ApJS, 64, 643
Sharma, M., McNamara, B. R., Nulsen, P. E. J., et al. 2004, ApJ, 613, 180
Skibba, R. A., van den Bosch, F. C., Yang, X., et al. 2011, MNRAS, 410, 417
Soker, N., & Pizzolato, F. 2005, ApJ, 622, 847
Sutherland, R. S., & Dopita, M. A. 1993, ApJS, 88, 253
Temi, P., Brighenti, F., Mathews, W. G., & Bregman, J. D. 2004, ApJS, 151, 237
van den Bosch, F. C., Weinmann, S. M., Yang, X., et al. 2005, MNRAS, 361, 1203
Van Dokkum, P. G., & Franx, M. 1995, AJ, 110, 2027
Vikhlinin, A., Markevitch, M., Murray, S. S., et al. 2005, ApJ, 628, 655
Voit, G. M., Donahue, M., Bryan, G. L., & McDonald, M. 2015, Natur, 519, 203